



Full length article

Tri(Fe/N/F)-doped mesoporous carbons as efficient electrocatalysts for the oxygen reduction reaction

Young-Geun Lee^a, Hyo-Jin Ahn^{a,b,*}^a Department of Materials Science and Engineering, Seoul National University of Science and Technology, Seoul 01811, Republic of Korea^b Program of Materials Science & Engineering, Convergence Institute of Biomedical Engineering and Biomaterials, Seoul National University of Science and Technology, Seoul 01811, Republic of Korea

ARTICLE INFO

Keywords:

Tri-doped mesoporous carbons
 Non-precious metal electrocatalysts
 Specific surface area
 Long-term stability
 Oxygen reduction reaction

ABSTRACT

In recent years, advanced designs of non-precious electrocatalysts, such as those with transition metals and heteroatoms into iron-nitrogen-doped mesoporous carbon, have been actively studied to replace precious-metal electrocatalysts for oxygen reduction reaction (ORR), which are used by future energy storage and conversion devices such as metal-air batteries and fuel cells. In the present study, we propose a noble non-precious electrocatalyst through the introduction of fluorine into iron-nitrogen doped mesoporous carbon. To this end, we synthesized Tri(Fe/N/F)-doped mesoporous carbon nanofiber (MCNF) using electrospinning, the precursor coating method, and carbonization. Tri(Fe/N/F)-doped MCNFs exhibited an improved onset potential of ~ 0.9 V, the half-wave potential of ~ 0.82 V, and limiting-current density of -4.76 mA cm⁻¹, with a four-electron pathway. In addition, Tri(Fe/N/F)-doped MCNFs showed remarkable long-term stability and endurance of methanol-crossover. Therefore, Tri(Fe/N/F)-doped MCNFs exhibited improved ORR performance, which could be explained by the increased specific surface area by mesoporous structures and improved oxygen adsorption by the synergy effects by Fe-N_x macrocycles and a high pyridinic- and pyrrolic-N species resulting from F doping.

1. Introduction

Oxygen reduction reaction (ORR) has recently become an object of considerable interest as important cathodic reaction in electrochemical energy conversion and storage devices such as fuel cells and rechargeable metal-air batteries with high energy density [1–4]. It is well-known that platinum (Pt)-based electrocatalysts promote sluggish kinetics of the ORR process. However, Pt-based electrocatalysts have shown low long-term stability, high overpotential, and low ORR efficiency, which necessitates further research aimed at finding stable, inexpensive, and efficient alternatives of electrocatalysts for ORR [5–10]. Accordingly, non-precious metal electrocatalysts (NPMCs) with improved ORR activity, such as metal-free heteroatom-doped carbon (i.e., nitrogen (N), sulfur (S), boron (B), phosphorous (P), and their multiple-doped carbon), transition metal complex (i.e., nitride, sulfide, and carbide), and transition metal-N_x compounds, have been studied to overcome the critical issues for the Pt-based electrocatalysts [11–18]. Specifically, transition metal-N doped carbon (M/N-C, M = iron (Fe), cobalt (Co), nickel (Ni), and copper (Cu)) have attracted considerable interest and have become the most promising ORR electrocatalysts due

to their high ORR activity in an alkaline medium. The ORR activity of the electrocatalysts was attributed by the sort of metal in the following order: Fe > Co > Ni > Cu [19–25]. In addition, good electrocatalysts possess an optimal pore structure, high surface area, and graphitic carbon which can provide efficient electron pathway, improved active site, and high electric conductivity for ORR, respectively. Therefore, advanced design of ORR electrocatalysts with the above-mentioned properties is inevitable.

Recently, in order to design ORR electrocatalysts, numerous studies have sought to apply to the heteroatom into M/N-C to improve the ORR activity. The heteroatoms (such as B, S, P, and F) doped carbons have demonstrated an enhanced ORR performance with a reduced overpotential, improved long-term stability, and efficient O₂ adsorption. In addition, the heteroatoms and nitrogen co-doped carbons showed an excellent ability to adsorb O₂ through the synergistic effect between the heteroatoms and nitrogen, leading to an improved ORR activity [26–29]. However, research on tri-doped mesoporous carbon including N and F species around the Fe-containing catalytic active sites for high-efficient ORR has not yet been undertaken.

The present study is the first to propose the synthesis of tri

* Corresponding author at: Program of Materials Science & Engineering, Convergence Institute of Biomedical Engineering and Biomaterials, Seoul National University of Science and Technology, Seoul 01811, Republic of Korea.

E-mail address: hjahn@seoultech.ac.kr (H.-J. Ahn).

<https://doi.org/10.1016/j.apsusc.2019.05.095>

Received 10 April 2019; Received in revised form 7 May 2019; Accepted 8 May 2019

Available online 09 May 2019

0169-4332/ © 2019 Elsevier B.V. All rights reserved.

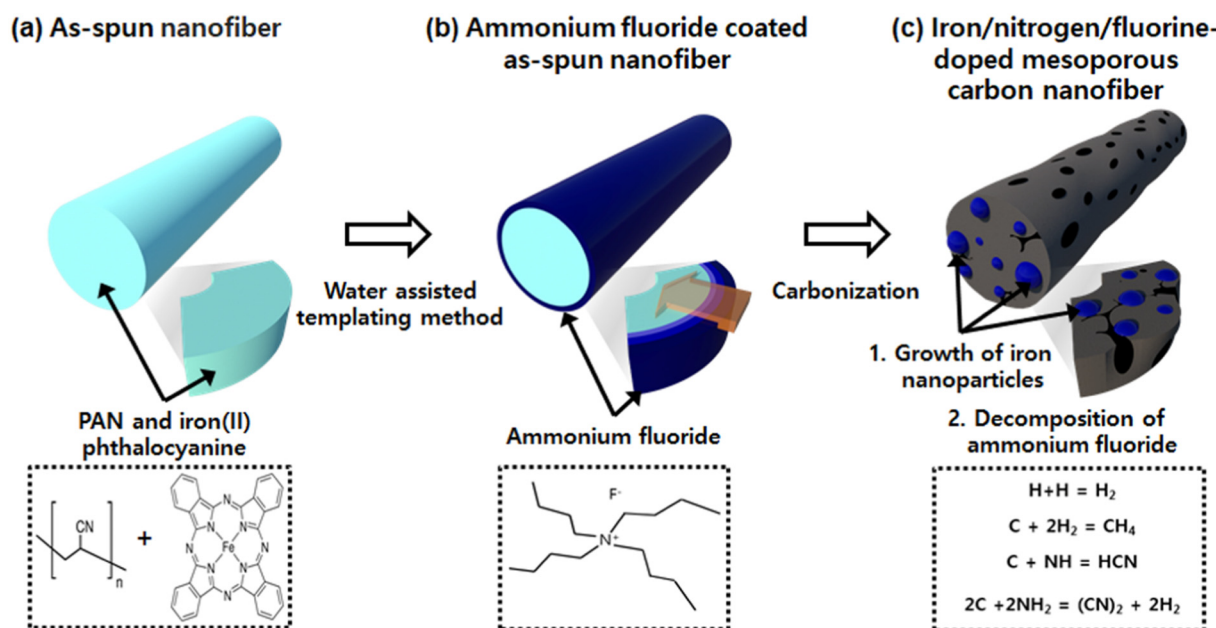


Fig. 1. Illustration scheme of the synthetic route for Tri(Fe/N/F)-doped MCNFs.

(nitrogen/fluorine/iron)-doped mesoporous carbon nanofibers (MCNFs) as a high efficient ORR electrocatalysts in the alkaline medium. In addition, one-dimensional CNFs with interlinked network, which could be an effective electron transfer for ORR, were used [30–32]. Finally, we also evaluate the ORR performance, long-term stability, and endurance of methanol-cross-over as electrocatalysts for Tri(Fe/N/F)-doped MCNFs in alkaline medium.

2. Experimental

2.1. Chemicals

Polyacrylonitrile (PAN, $M_w = 150,000$), iron(II) phthalocyanine ($\text{C}_{32}\text{H}_{16}\text{FeN}_8$), *N,N*-dimethylformamide (DMF, 99.8%), ammonium fluoride (NH_4F , 98%), ethanol ($\text{C}_2\text{H}_6\text{O}$), hydrofluoric acid (HF), Nafion® perfluorinated resin solution, 2-propanol, and potassium hydroxide were purchased from Sigma-Aldrich. All chemicals were used without further purification.

2.2. Synthesis of Tri(Fe/N/F)-doped MCNFs

Tri(Fe/N/F)-doped MCNFs were synthesized using electrospinning, the precursor coating method, and carbonization. First, 10 wt% PAN and 8 wt% iron(II) phthalocyanine were mixed in the DMF solution to synthesize the as-spun nanofibers. The electrospinning process was performed at the feeding rate of 0.03 mL h^{-1} and the applied voltage of 13 kV under the humidity of 15% in a chamber. To dope the fluorine precursors on the surface of CNFs, as-spun nanofibers were added into a mixed solution of NH_4F , distilled water, and ethanol and then stirred for 12 h and dried at 50°C in a vacuum oven for 12 h. The fluorine precursors coated as-spun nanofibers were stabilized at 250°C in air, and then carbonization was carried out at 800°C under nitrogen for 2 h. After carbonization, in order to remove the inorganic species of Fe precursors, the sample was washed by 10 wt% HF. Finally, we successfully synthesized Tri(Fe/N/F)-doped MCNFs (Fe/N/F-MCNFs). For comparison, nitrogen-doped carbon nanofibers (N-CNFs) without $\text{C}_{32}\text{H}_{16}\text{FeN}_8$ and the coating method of fluorine precursors, iron and nitrogen co-doped carbon nanofibers (Fe/N-CNFs) without the coating method of fluorine precursors, and the conventional Pt/C (20 wt% Pt on Vulcan carbon, De Nora S.P.A.) were prepared.

2.3. Characterizations

The structures and morphologies of all samples were examined using field-emission scanning electron microscopy (FE-SEM, Hitachi S-4800) and transmission electron microscopy (MULTI/TEM; Tecnai G², KBSI Gwangju Center). In addition, in order to demonstrate the distribution of all elements, energy-dispersive spectrometry (EDS)-mapping was performed. X-ray diffractometry analyses (XRD, Rigaku D/Max 2500 V) with the $\text{Cu K}\alpha$ radiation between 10° and 90° with the step size of 0.02° were performed. The Raman spectra (JASCO NRS-5100) were obtained using the laser-excitation wavelength of 532.1. To investigate the surface area and pore structure of the samples, the Brunauer-Emmett-Teller (BET) was measured using nitrogen adsorption and desorption at 77 K. X-ray photoelectron analyses (XPS, ESCALAB 250) with an Al $\text{K}\alpha$ X-ray sources were performed so as to identify the chemical properties on the surface or the samples. Furthermore, C 1s core level (284.5 eV) was applied to calibrate the binding energies of the XPS spectra.

2.4. Electrochemical measurements

Electrochemical performance measurements were performed using a potentiostat/galvanostat (Ecochemie Autolab PGST302N) with a three-electrode system composed of the reference electrode (Ag/AgCl, sat. KCl), the counter electrode (Pt wire), and the working electrode (glassy carbon, rotating disk electrode (RDE)). Potentials of all electrodes were calibrated into RHE [33–35]. To measure the ORR performance, electrocatalyst inks were prepared by mixing 20 wt% Nafion and 80 wt% electrocatalyst in 2-propanol and then loaded onto the RDE and dried at 50°C . Cyclic voltammogram (CV) and lineal sweep voltammogram (LSV) were performed in an O_2 -saturated 0.1 M KOH electrolyte to evaluate the ORR activities. During the LSV, various rotational speeds of 400, 900, 1600, and 2500 rpm (RPM) were applied at the scan rate of 5 mV s^{-1} . In addition, Koutechy-Levich (K-L) plots were used to evaluate the transferred electron number (n). The long-term stability measurements were performed in the range of 0.4 V to 0.9 V in an O_2 -saturated 0.1 M KOH electrolyte for 10,000 cycles at the scan rate of 50 mV s^{-1} ; then, the LSV was carried out at 1600 rpm in an O_2 -saturated 0.1 M KOH electrolyte. For the methanol endurance during the ORR process, O_2 -saturated 0.1 M KOH with 0.5 M CH_3OH electrolyte

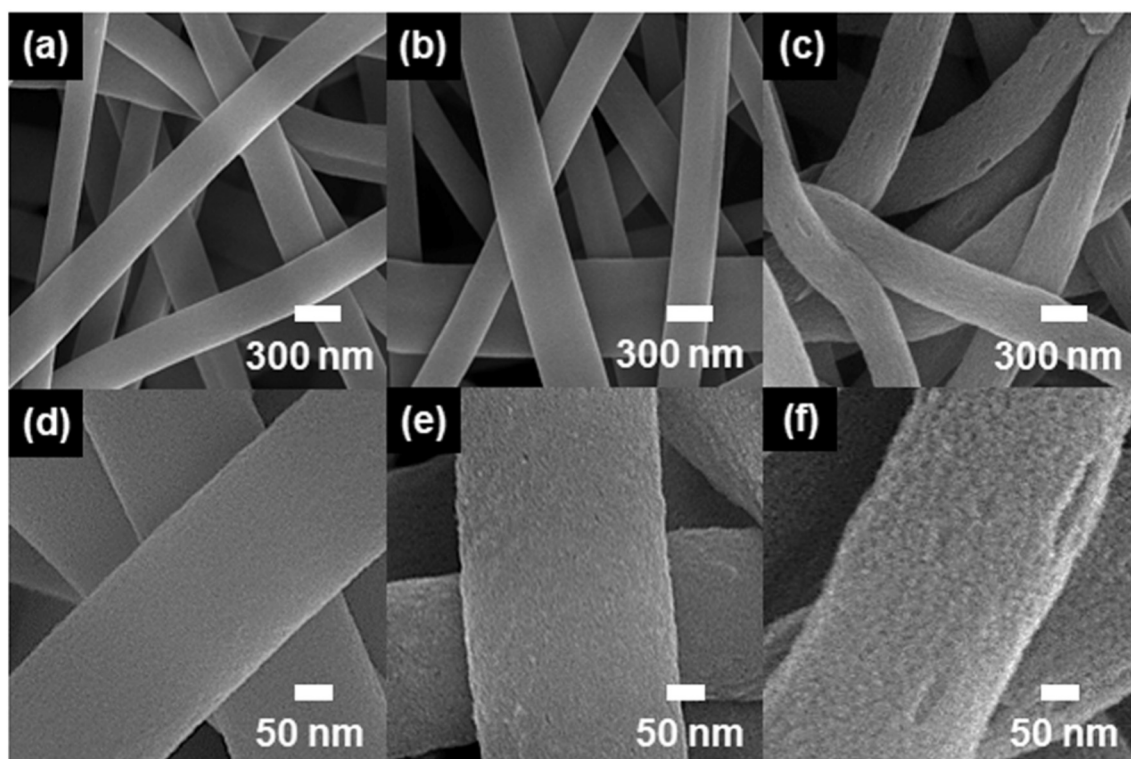


Fig. 2. (a–c) Low-resolution and (d–f) high-resolution FESEM images of N-doped CNFs, Co(Fe/N)-doped CNFs, and Tri(Fe/N/F)-doped MCNFs.

was used.

3. Results and discussion

Fig. 1 shows a schematic illustration of the synthetic process for the Tri(Fe/N/F)-doped MCNFs. First, the as-spun nanofibers consisting of polyacrylonitrile (PAN, $M_w = 150,000$) and iron(II) phthalocyanine ($C_{32}H_{16}FeN_8$) were manufactured by the electrospinning technique (Fig. 1(a)); thereafter, the as-spun nanofibers were dipped in the ammonium fluoride (NH_4F) solution to dope the NH_4F on the surface (see Fig. 1(b)). Finally, Tri(Fe/N/F)-doped MCNFs were synthesized by carbonization at $800^\circ C$ under nitrogen (see Fig. 1(c)). In particular, Fig. 1(c) displays the formation of mesoporous structure on the surface of the CNFs, which can be explained by the decomposition of NH_4F and growth of Fe nanoparticles with an increase of the temperature. The NH_4F can be decomposed into H, NH, and NH_2 radicals which can combine with carbon and produce methane (CH_4), hydrogen cyanide (HCN), and cyanogen(CN)₂, respectively, leading to the formation of a mesoporous structure on the surface of the CNFs [36,37].

Fig. 2 shows low-resolution (Fig. 2(a)–(c)) and high-resolution (Fig. 2(d)–(f)) FE-SEM images of N-doped CNFs, Co(Fe/N)-doped CNFs, and Tri(Fe/N/F)-doped MCNFs. All samples exhibited one-dimensional nanostructures with interlinked networks which can effectively transfer electrons, leading to an improved ORR performance. N-doped CNFs (Fig. 2(a) and (d)) exhibited a smooth surface without any pores on their surface as compared to Co(Fe/N)-doped CNFs (Fig. 2(b) and (e)) and Tri(Fe/N/F)-doped MCNFs (Fig. 2(c) and (f)) with a relatively rough surface. This finding could be attributed to the growth of Fe nanoparticles during carbonization. In addition, as compared to N-doped CNFs of 225–253 nm in diameter, Co(Fe/N)-doped CNFs of 282–318 nm in diameter and Tri(Fe/N/F)-doped MCNFs of 271–302 nm in diameter exhibited an increase of diameters due to the embedded Fe nanoparticles. In particular, due to the synergy effect of the growth of embedded Fe nanoparticles and the decomposition of NH_4F during carbonization, which can provide an efficient electron pathway and increased active sites, resulting in the improvement of ORR activity, Tri

(Fe/N/F)-doped MCNFs showed distinct mesoporous structures on the CNF surface.

In order to further investigate the structural properties using low-resolution and high-resolution images of Tri(Fe/N/F)-doped MCNFs, the TEM analyses were performed. Fig. 3(a)–(b) shows well-dispersed Fe nanoparticles with relative dark spots, smaller than ~ 23 nm in size and embedded in carbon nanofibers. In addition, rough surfaces and mesoporous structures of the CNFs, formed by a synergistic effect of the growth of Fe nanoparticles and the decomposition of NH_4F during carbonization, were observed. The high-resolution TEM image (see Fig. 3(c)) showed a lattice distance of the Fe nanoparticle and carbon with ~ 0.21 nm and ~ 0.34 nm which correspond to the (111) plane of Fe and the (002) plane of graphitic carbon, respectively. In particular, the partial graphitization is attributed by Fe nanoparticles, as the existence of Fe can crystallize carbon, thereby leading to an increase of electrical conductivity of amorphous carbon [38,39]. To demonstrate the content distribution of carbon, nitrogen, fluorine, and iron in Tri(Fe/N/F)-doped MCNFs, TEM-EDS mapping was performed (see Fig. 3(d)). The EDS data imply that the elements are well dispersed along the CNF, indicating that N, F, and Fe are uniformly doped in CNFs.

To further investigate the crystal properties of N-doped CNFs, Co(Fe/N)-doped CNFs, and Tri(Fe/N/F)-doped MCNFs, the XRD and Raman spectra measurements were performed (see Fig. 4(a)–(b)). For the XRD data in Fig. 4(a), all samples displayed peaks around 25° and 44° , corresponding to the (002) and (101) planes of graphitic carbon (JCPDS card No. 41-1487), respectively [40–42]. In addition, Co(Fe/N)-doped CNFs and Tri(Fe/N/F)-doped MCNFs had peaks of 45° , which corresponds to (110) plane of pure Fe with body-centered structure (JCPDS card No. 87-0721). More specifically, the peaks relative to the graphite of Co(Fe/N)-doped CNFs and Tri(Fe/N/F)-doped MCNFs were relatively sharper and shifted to high diffraction angle as compared to N-doped CNFs, implying that the crystallization of carbon occurred due to the existence of Fe precursor during the carbonization process. As shown in Fig. 4(b), the Raman spectra of N-doped CNFs, Co(Fe/N)-doped CNFs, and Tri(Fe/N/F)-doped MCNFs exhibited two distinctive

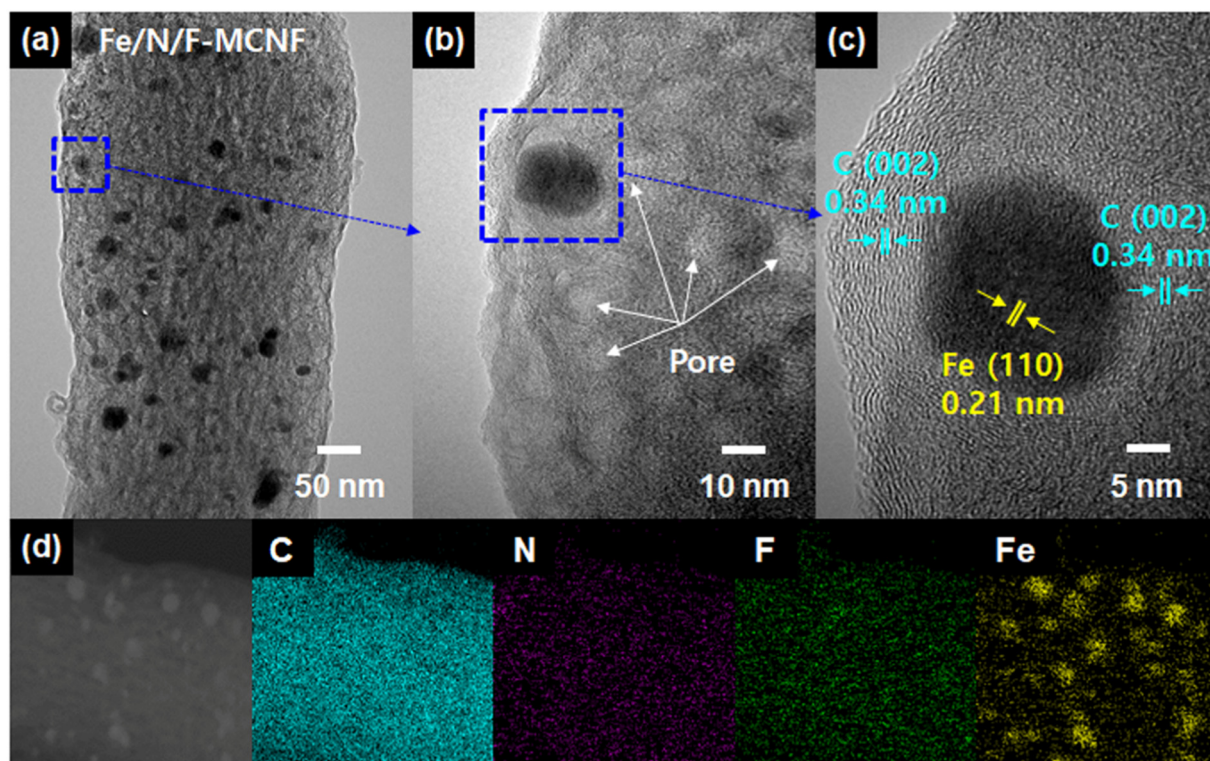


Fig. 3. (a) Low-resolution, (b) and (c) high-resolution TEM images, and (d) TEM-EDS mapping results of Tri(Fe/N/F)-doped MCNFs.

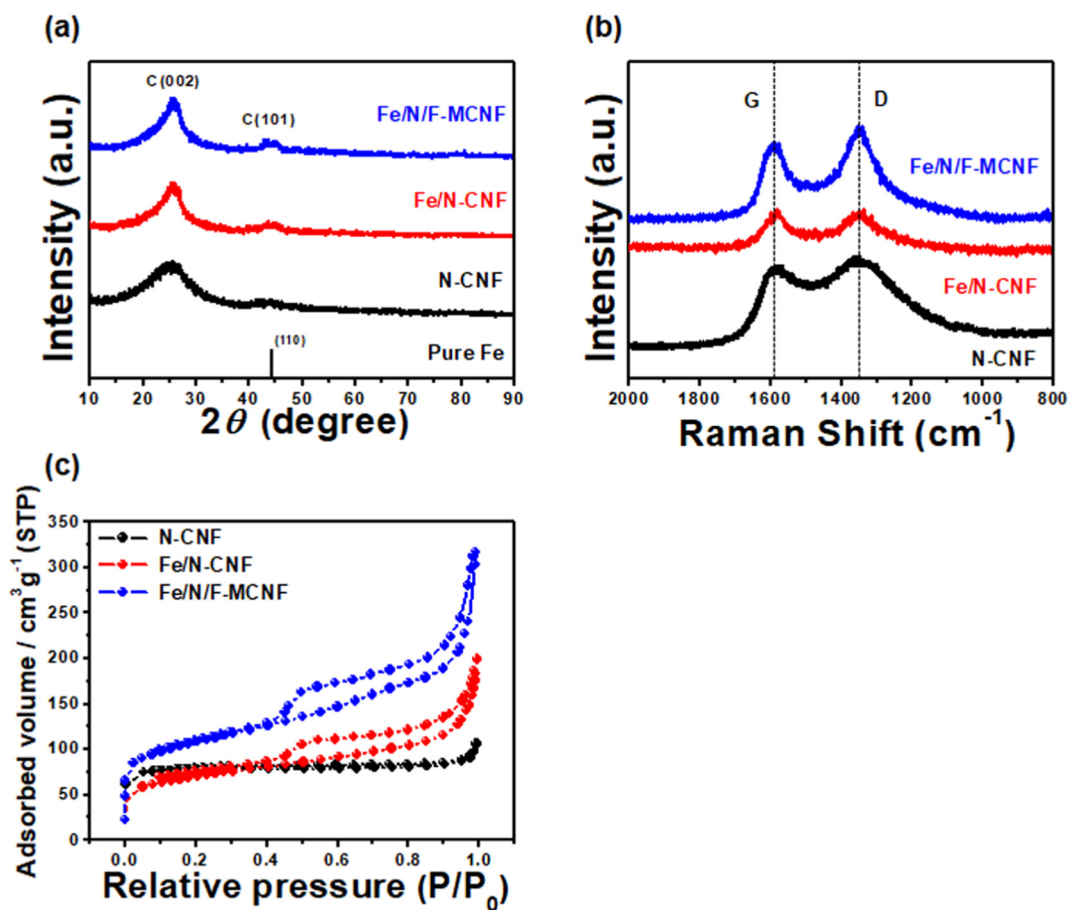


Fig. 4. (a) XRD patterns, (b) Raman spectra, and (c) N₂ adsorption/desorption isotherms of N-doped CNFs, Co(Fe/N)-doped CNFs, and Tri(Fe/N/F)-doped MCNFs.

Table 1

Specific surface area, total pore volume, average pore diameter, and pore volume fraction of N-doped CNFs, Co(Fe/N)-doped CNFs, and Tri(Fe/N/F)-doped MCNFs.

Samples	S_{BET} [$\text{m}^2 \text{g}^{-1}$]	Total pore volume ($p/p_0 = 0.990$) [$\text{cm}^3 \text{g}^{-1}$]	Average pore diameter [nm]	Pore volume fraction	
				V_{micro} (%)	V_{meso} (%)
N-CNF	304.9	0.16	2.0	94.39	5.61
Fe/N-CNF	301.4	0.28	4.6	68.60	31.40
Fe/N/F-MCNF	480.6	0.48	5.1	64.24	35.76

peaks of D-band at $\sim 1350 \text{ cm}^{-1}$ and G-band at $\sim 1596 \text{ cm}^{-1}$, which can be directly related to the existence of structural disorder in the carbon lattice due to heteroatomic doping effect, and the E_{2g} vibration state in sp^2 bonded carbon atoms corresponded to the graphitic carbon, respectively. Therefore, the intensity ratio of D-band and G-band ($I_{\text{D}}/I_{\text{G}}$) can determine the degree of the doping effect and graphitization [43,44]. The $I_{\text{D}}/I_{\text{G}}$ of N-doped CNFs, Co(Fe/N)-doped CNFs, and Tri(Fe/N/F)-

N/F)-doped MCNFs amounted to 1.00, 0.98, and 1.02, respectively. While the decreased $I_{\text{D}}/I_{\text{G}}$ can be attributed to a partial graphitization of carbon around the Fe nanoparticles, the increased $I_{\text{D}}/I_{\text{G}}$ relates to the fluorine doping effect whereby fluorine atoms into the carbon structure induce the generation of structural defects. To identify the specific surface areas and porous structures of N-doped CNFs, Co(Fe/N)-doped CNFs, and Tri(Fe/N/F)-doped MCNFs, nitrogen adsorption/desorption isotherms using the BET measurements were analyzed (see Fig. 4(c)). In general, the isotherm of the N-doped CNFs exhibits type I characteristic based on International Union of Pure and Applied Chemistry, indicating that the N-doped CNFs possesses microporous structure (pore width, $< 2 \text{ nm}$) [30]. On the other hand, the isotherms of Co(Fe/N)-doped CNFs and Tri(Fe/N/F)-doped MCNFs show type IV characteristic, implying that they possess a mesoporous structure (pore width, $2\text{--}50 \text{ nm}$) at a high pressure ($P/P_0 > 0.4$). This can be attributed to the growth of Fe nanoparticle and the decomposition of NH_4F during carbonization. Table 1 provides further detail on the BET results with the specific surface areas, total pore volumes, average pore diameters, and pore volume fractions. As compared to N-doped CNFs and Co(Fe/N)-

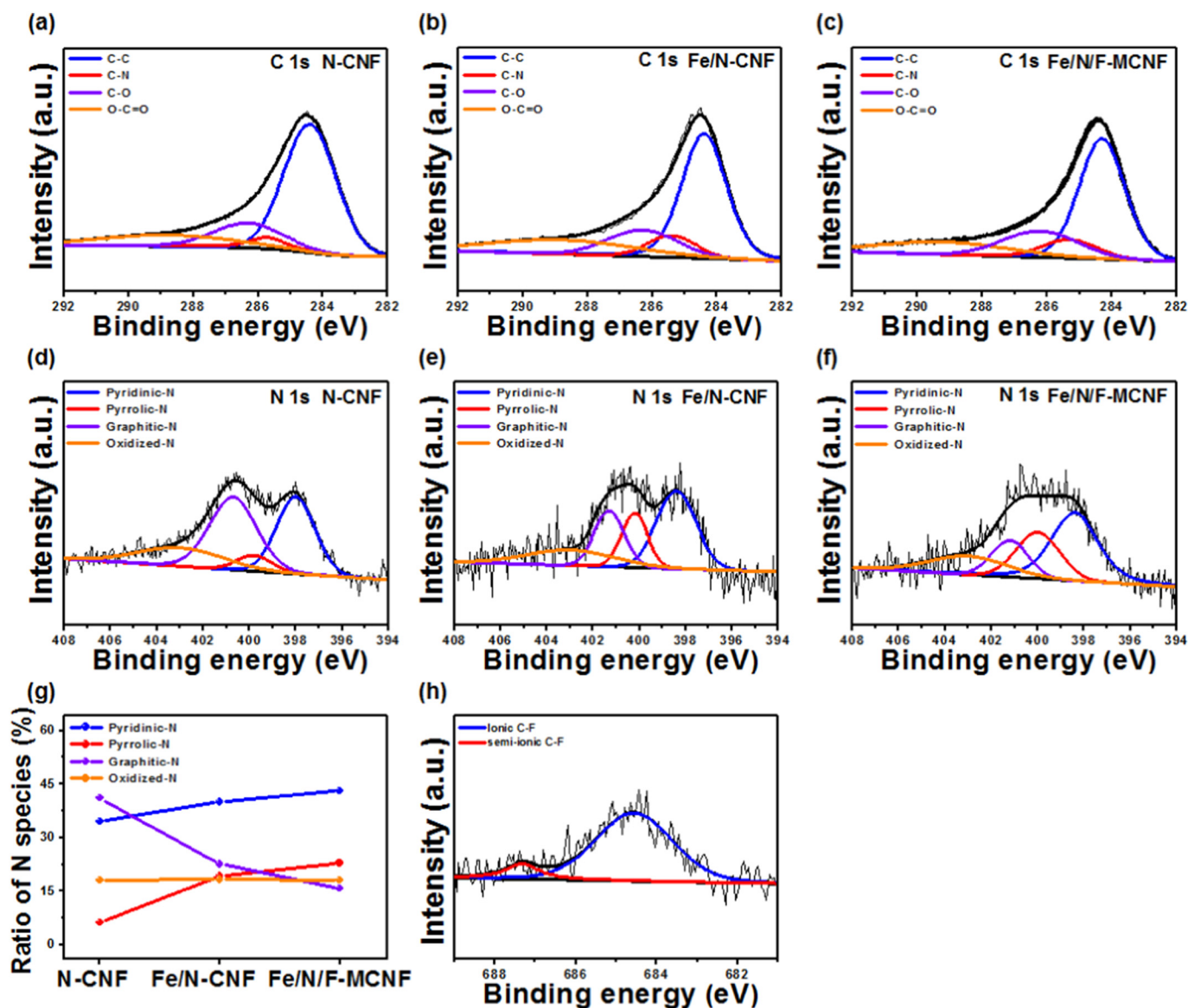


Fig. 5. XPS spectra of C 1s of (a) N-doped CNFs, (b) Co(Fe/N)-doped CNFs, and (c) Tri(Fe/N/F)-doped MCNFs and N 1s of (d) N-doped CNFs, (e) Co(Fe/N)-doped CNFs, and (f) Tri(Fe/N/F)-doped MCNFs. (g) Comparison of N species of N-doped CNFs, Co(Fe/N)-doped CNFs, and Tri(Fe/N/F)-doped MCNFs. (h) XPS spectra of F 1s of Tri(Fe/N/F)-doped MCNFs.

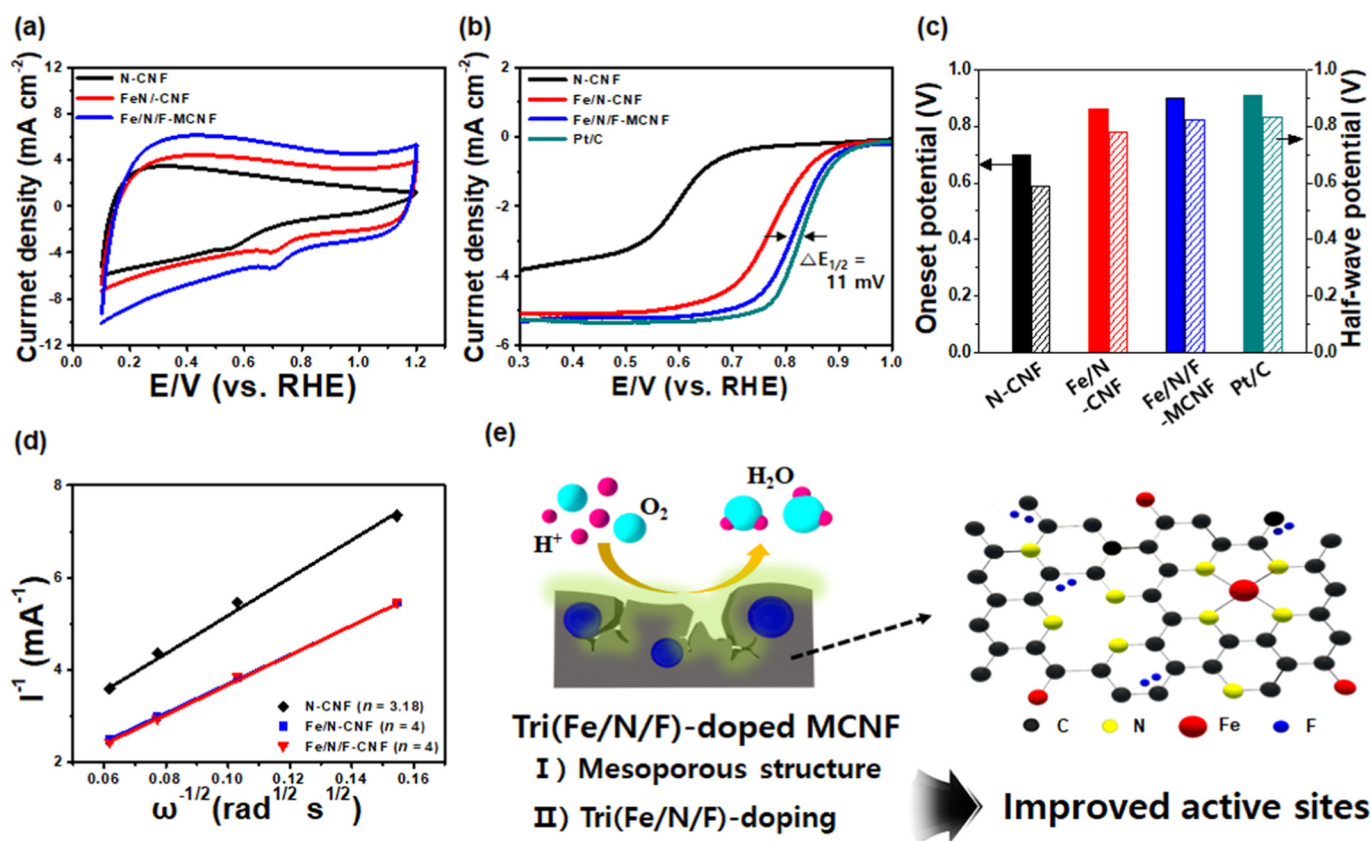


Fig. 6. (a) CV curves of N-doped CNFs, Co(Fe/N)-doped CNFs, and Tri(Fe/N/F)-doped MCNFs. (b) LSV curves of N-doped CNFs, Co(Fe/N)-doped CNFs, and Tri(Fe/N/F)-doped MCNFs, and commercial Pt/C. (c) Comparison of the onset potential and the half-wave potential of N-doped CNFs, Co(Fe/N)-doped CNFs, Tri(Fe/N/F)-doped MCNFs, and commercial Pt/C from LSV curves. (d) K-L plots of N-doped CNFs, Co(Fe/N)-doped CNFs, and Tri(Fe/N/F)-doped MCNFs at 0.6 V. (e) Schematic illustration of improved active site for Tri(Fe/N/F)-doped MCNFs.

doped CNFs, the Tri(Fe/N/F)-doped MCNFs exhibited the highest specific surface area ($480.6 \text{ m}^2 \text{ g}^{-1}$), total pore volume ($0.48 \text{ cm}^3 \text{ g}^{-1}$), average pore diameter (5.1 nm), and mesopore volume fraction (35.76%). The improved properties of Tri(Fe/N/F)-doped MCNFs could be a significant factor that offers an efficient electron pathway and high active sites for the ORR.

The XPS measurements were performed to investigate the chemical bond states on the carbon surface of N-doped CNFs, Co(Fe/N)-doped CNFs, and Tri(Fe/N/F)-doped MCNFs. C 1s spectra of the N-doped CNFs (Fig. 5(a)), Co(Fe/N)-doped CNFs (Fig. 5(b)) and Tri(Fe/N/F)-doped MCNFs (Fig. 5(c)) showed four peaks of C–C (284.5 eV), C–N (285.6 eV), C–O (286.1 eV), and O–C=O (288.8 eV). More specifically, Co(Fe/N)-doped CNFs and Tri(Fe/N/F)-doped MCNFs exhibited an increased volume ratio of C–N bonds as compared to N-doped CNFs due to a high nitrogen-containing Fe precursor (see Table S1). For N 1s spectra of the samples in Fig. 5(d)–(f), the decomposition of N 1s spectra exhibited four signals peaking at $403.0 \pm 0.3 \text{ eV}$, $401.0 \pm 0.3 \text{ eV}$, $400.0 \pm 0.3 \text{ eV}$, and $398.4 \pm 0.3 \text{ eV}$, which corresponding to oxidized-N, graphitic-N, pyrrolic-N, and pyridinic-N, respectively. As shown in Fig. 5(g), N-doped CNFs showed a higher ratio of graphitic-N than Co(Fe/N)-doped CNFs and Tri(Fe/N/F)-doped MCNFs, whereas the ratio of pyrrolic-N and pyridinic-N gradually increased from Co(Fe/N)-doped CNFs to Tri(Fe/N/F)-doped MCNFs. This increase can be attributed to the following two factors: (i) the high nitrogen-containing Fe can exist as Fe-N_x macrocycles in the carbon structure, leading to an increase of the ratio of pyrrolic-N and pyridinic-N; and (ii) introduction of F atoms into the carbon matrix can produce structural defects, implying that F doping can break the graphitic bonds and then cause a high ratio of pyrrolic-N and pyridinic-N. In this connection, the pyrrolic-N and pyridinic-N can enhance the ORR activity

due to two and one electron per a π -system, respectively [45–47]. In addition, Fe- N_x macrocycles in the carbon structure could more effectively deduct an electron, so that carbon becomes a positive charge and thus efficiently adsorbs oxygen [40,48,49]. Fig. 5(h) shows F 1s spectra of Tri(Fe/N/F)-doped MCNFs. The F 1s spectra were divided into two peaks at 684.8 eV and 687.5 eV, which correspond to ionic C–F bonds and semi-ionic C–F, respectively [44]. The doping of F induces the carbon to possess a positive charge and improves the activity of π -electrons in carbon, resulting in an improved adsorption of oxygen and the ORR activity. Furthermore, several previous studies have demonstrated the following ORR activity order for C–F bonds: ionic C–F > semi-ionic C–F > covalent C–F [50,51].

To further evaluate the electrochemical properties of N-doped CNFs, Co(Fe/N)-doped CNFs, and Tri(Fe/N/F)-doped MCNFs, CVs were measured in O_2 -saturated 0.1 M KOH electrolyte at the scan rate of 50 mV s^{-1} (see Fig. 6(a)). Oxygen reduction peak potentials of N-doped CNFs, Co(Fe/N)-doped CNFs, and Tri(Fe/N/F)-doped MCNFs were 0.653, 0.688, and 0.713 V, respectively. High potential of oxygen reduction peaks is directly related to the high ORR activity. Therefore, Tri(Fe/N/F)-doped MCNFs indicated the highest ORR activity. In Fig. S1, obvious oxygen reduction peaks as compared to CVs in Ar- and O_2 -saturated KOH electrolyte can be observed. The linear sweep voltammetry (LSV) measurement on the RDE was used to investigate the ORR electrochemical kinetics in O_2 -saturated KOH electrolyte at the rotating speed of 1600 rpm and the scan rate of 5 mV s^{-1} . Tri(Fe/N/F)-doped MCNFs displayed an improved on-set potential of $\sim 0.900 \text{ V}$, half-wave potential ($E_{1/2}$) of $\sim 0.822 \text{ V}$, and limiting-current density of $\sim 5.23 \text{ mA cm}^{-2}$ at 0.6 V. These results indicate that it is almost identical to the commercial Pt/C, as Tri(Fe/N/F)-doped MCNFs exhibited a gap only 11 mV, 10 mV, and 0.08 mA cm^{-2} as compared to Pt/C

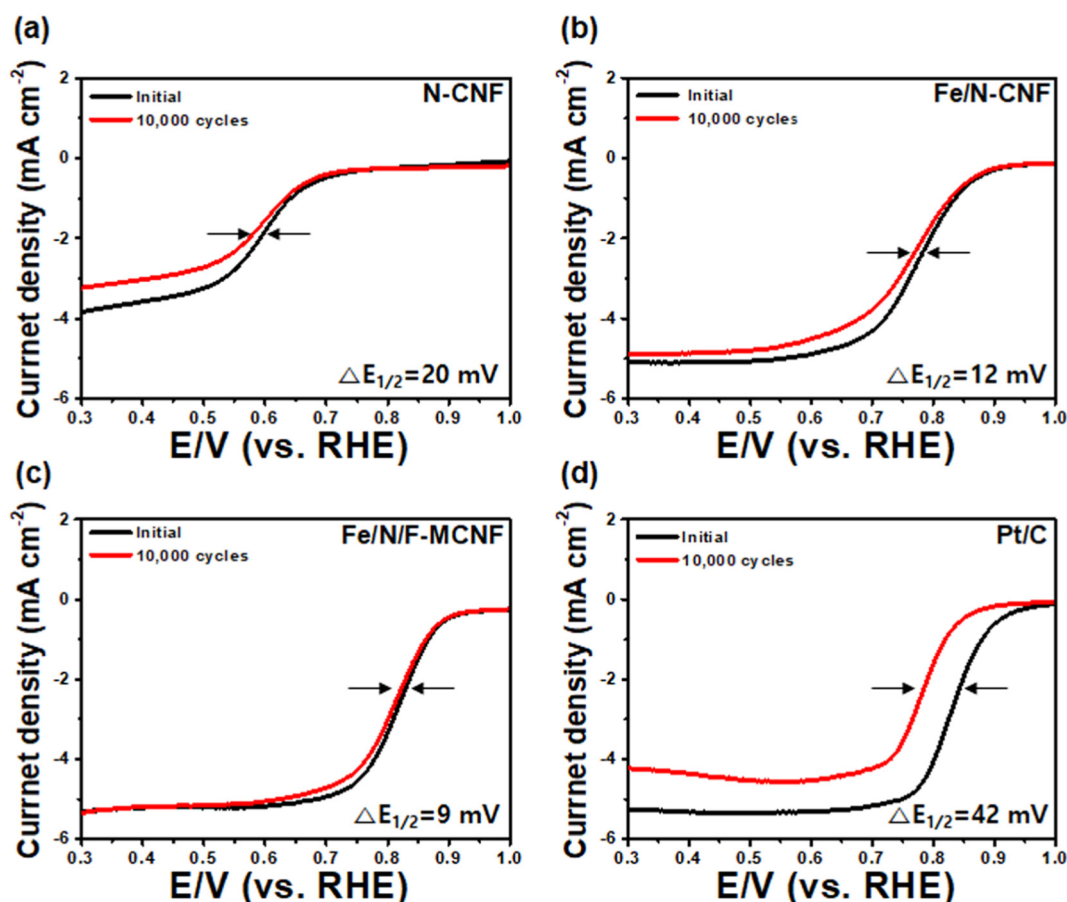


Fig. 7. LSV curves of (a) N-doped CNF, (b) Co(Fe/N)-doped CNF (c) Tri(Fe/N/F)-doped MCNFs, and (d) commercial Pt/C with a scan rate of 5 mV s^{-1} before and after the stability test at a rotating speed of 1600 rpm in O_2 -saturated 0.1 M KOH.

with the on-set potential of $\sim 0.911 \text{ V}$, $E_{1/2}$ of $\sim 0.831 \text{ V}$ and the limiting-current density of -5.31 mA cm^{-2} at 0.6 V , respectively (see Fig. 6(b)–(c)). In addition, as compared to N-doped CNFs and Co(Fe/N)-doped CNFs, Tri(Fe/N/F)-doped MCNFs exhibited an enhanced ORR activity with a superior on-set potential, $E_{1/2}$, and limiting-current density. This outcome can be ascribed to the following two reasons: (i) increased specific surface area by mesoporous structures; and (ii) improved oxygen adsorption by the synergy effects by Fe- N_x macrocycles and a high pyridinic- and pyrrolic-N species resulting from F doping. Fig. S2 shows the polarization curves of Tri(Fe/N/F)-doped MCNFs from 400 to 2500 rpm. The current density gradually decreased with the increase of rotating speed, which can be ascribed to the shortened diffusion layer [6]. In general, the ORR process in alkaline medium can be explained by two possible pathways with two- and four-electron reduction pathway. Of them, four-electron pathway is more advantageous for a high ORR performance. Based on the polarization curves at various rotation speeds, the transferred electron number (n) can be calculated from the Koutecky-Levich (K-L) as following equation: [19].

$$\frac{1}{j} = \frac{1}{j_k} + \frac{1}{j_d} = -\frac{1}{nFkC_0^b} - \frac{1}{0.62nFD_0^{2/3}\nu^{-1/6}C_0^b\omega^{1/2}}$$

where j is the measured current density, j_k is kinetic-limiting current density, j_d is the diffusion-limiting current density, F is Faraday constant ($96,485 \text{ C mol}^{-1}$), k is electron transfer rate constant, and C_0 is bulk concentration ($1.2 \times 10^{-6} \text{ mol cm}^{-3}$), D_0 is bulk concentration of O_2 ($1.2 \times 10^{-6} \text{ mol cm}^{-3}$) in 0.1 M KOH solutions, ν is kinetic viscosity ($1.1 \times 10^{-2} \text{ cm}^2 \text{ s}^{-1}$), and ω is angular velocity of the electrode [6,40]. The K-L plot of Tri(Fe/N/F)-doped MCNFs shows an excellent linearity with the four-electron reduction pathway in the potential ranging from

0.3 and 0.6 V (vs. RHE) (see Fig. S2). In addition, the K-L plots and the n values of all samples, which amounted to 0.6 V, exhibited a good linearity, and 3.18, 4, and 4 for N-doped CNFs, Co(Fe/N)-doped CNFs, Tri(Fe/N/F)-doped MCNFs, respectively (see Fig. 6(d)). Therefore, Tri(Fe/N/F)-doped MCNFs as ORR electrocatalysts can generate a four-electron reduction pathway, leading to a superior ORR process in the alkaline medium.

The long-term stability measurements of the N-doped CNFs, Co(Fe/N)-doped CNFs, Tri(Fe/N/F)-doped MCNFs, and commercial Pt/C were performed from 0.4 V to 0.9 V in an O_2 -saturated 0.1 M KOH electrolyte for 10,000 cycles at the scan rate of 50 mV s^{-1} (see Fig. 7). After 10,000 cycles, Tri(Fe/N/F)-doped MCNFs showed a superior long-term stability with a relatively low negative shift in $E_{1/2}$ as compared to N-doped CNFs ($\sim 20 \text{ mV}$) and commercial Pt/C ($\sim 42 \text{ mV}$). The improved long-term stability can be attributed to Fe- N_x macrocycle which could facilitate the stable doping of nitrogen [52]. In particular, the methanol-crossover is a critical issue in direct methanol fuel cells (DMFCs), as the cathode is mixed by methanol flowed from the anode, which could hinder the ORR process. For the effect of the methanol-crossover, the LSV measurements in 0.5 M methanol-contained O_2 -saturated 0.1 M KOH electrolyte were performed (see Fig. 8). Almost no difference of the ORR performance between with and without methanol of the N-doped CNFs, Co(Fe/N)-doped CNFs, and Tri(Fe/N/F)-doped MCNFs was observed, indicating the excellent endurance of methanol-crossover as non-precious electrocatalysts. On the other hand, due to the methanol oxidation reaction in the cathodic potentials, commercial Pt/C showed a serious degradation of the ORR activity in the methanol-containing electrolyte.

Therefore, the remarkable electrochemical performance of Tri(Fe/N/F)-doped MCNFs in the ORR process can be explained by two

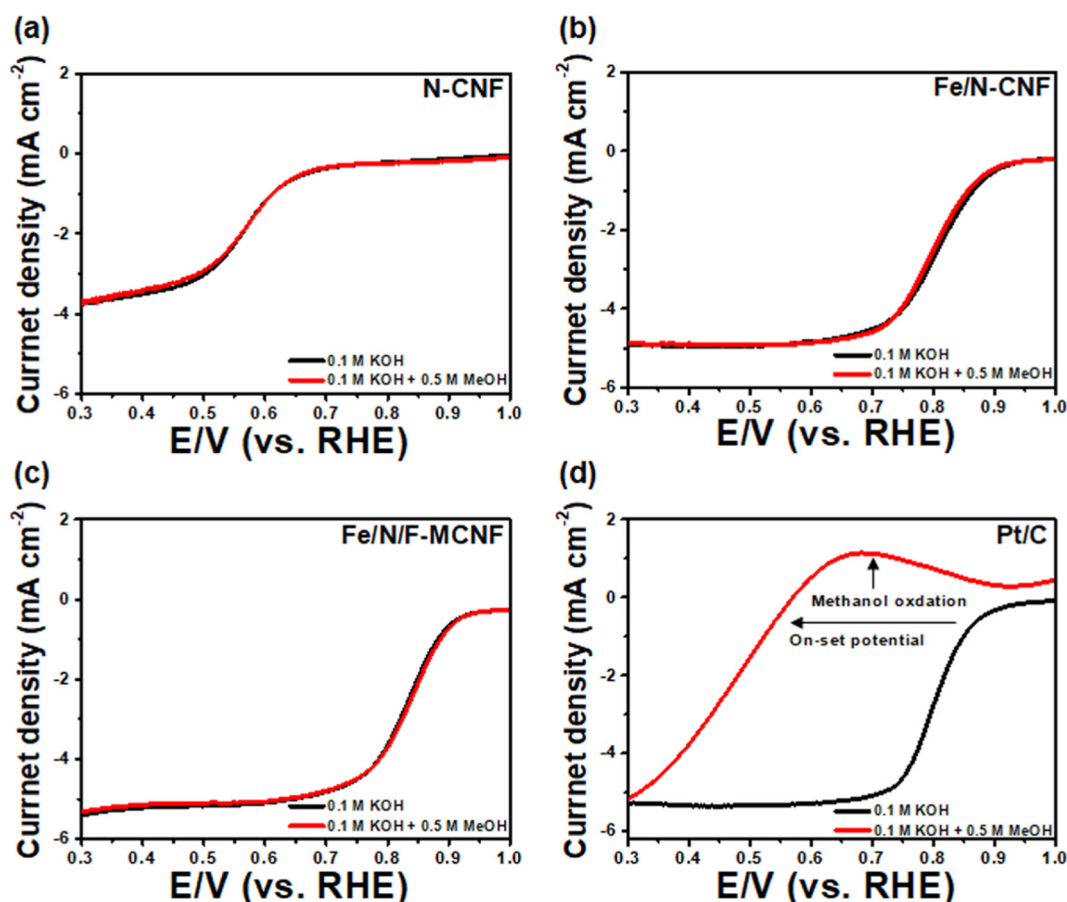


Fig. 8. LSV curves of (a) N-doped CNFs, (b) Co(Fe/N)-doped CNFs (c) Tri(Fe/N/F)-doped MCNFs, and (d) commercial Pt/C with a scan rate of 5 mV s^{-1} at a rotating speed of 1600 rpm in O_2 -saturated 0.1 M KOH with and without 0.5 M CH_3OH .

reasons. First, an increased specific surface area by mesoporous structures can offer improved active sites and efficient mass transfer. Secondly, an improved oxygen adsorption by the synergy effects by Fe-N_x macrocycles and a high pyridinic- and pyrrolic-N species resulting from F doping could result in the efficient ORR performance.

4. Conclusions

In the present study, Tri(Fe/N/F)-doped MCNFs as ORR electrocatalysts were fabricated using electrospinning, the precursor coating method, and carbonization. This study is the first to propose the introduction of fluorine as heteroatom into metal-nitrogen doped mesoporous carbon. Tri(Fe/N/F)-doped MCNFs exhibited a high specific surface area ($480.6 \text{ m}^2 \text{ g}^{-1}$), Fe-N_x macrocycles, and a high pyridinic- and pyrrolic-N species resulting from F doping. Thus, Tri(Fe/N/F)-doped MCNFs showed a remarkably improved ORR activities with the improved onset potential of $\sim 0.90 \text{ V}$, $E_{1/2}$ of $\sim 0.822 \text{ V}$, limiting-current density of -5.23 mA cm^{-1} at 0.6 V , with a four-electron path way. In addition, compared to commercial Pt/C, Tri(Fe/N/F)-doped MCNFs exhibited a superior long-term stability of the low negative shift of $\sim 9 \text{ mV}$ and an excellent endurance of methanol-crossover. To conclude, Tri(Fe/N/F)-doped MCNFs as non-precious electrocatalysts may be used as a promising candidate for applications such as metal-air batteries and fuel cells.

Acknowledgments

This study was supported by the Advanced Research Project funded by the SeoulTech (Seoul National University of Science and Technology).

Appendix A. Supplementary data

Supplementary data to this article can be found online at <https://doi.org/10.1016/j.apsusc.2019.05.095>.

References

- [1] J. Greeley, I.E.L. Stephens, A.S. Bondarenko, T.P. Johansson, H.A. Hansen, T.F. Jaramillo, J. Rossmeisl, I. Chorkendorff, J.K. Nørskov, *Nat. Chem.* 1 (2009) 552–556.
- [2] H.-G. Jung, J. Hassoun, J.-B. Park, Y.-K. Sun, B. Scrosati, *Nat. Chem.* 4 (2012) 579–585.
- [3] G.A. Ferrero, K. Preuss, A. Marinovic, A.B. Jorge, N. Mansor, D.J.L. Brett, A.B. Fuenes, M. Sevilla, M.-M. Titirici, *ACS Nano* 10 (2016) 5922–5932.
- [4] Z. Zhao, M. Li, L. Zhang, L. Dai, Z. Xia, *Adv. Mater.* 27 (2015) 6834–6840.
- [5] H. Tan, T. Li, X. Jiang, J. Tang, Z. Wang, H. Qian, P. Mei, V. Malgras, Y. Bando, Y. Yamauchi, *Nano Energy* 36 (2017) 286–294.
- [6] G.-H. An, E.-H. Lee, H.-J. Ahn, *J. Alloys Compd.* 682 (2016) 746–752.
- [7] D. Ji, S. Peng, J. Lu, L. Li, S. Yang, S. Ramakrishnan, *J. Mater. Chem. A* 5 (2017) 7507–7515.
- [8] J. Xiao, Y. Xia, C. Hu, J. Xi, S. Wang, *J. Mater. Chem. A* 5 (2017) 11114–11123.
- [9] B. Lu, T.J. Smart, D. Qin, J.E. Lu, N. Wang, L. Chen, Y. Peng, Y. Ping, S. Chen, *Chem. Mater.* 29 (2017) 5617–5628.
- [10] G.-H. An, Y.-G. Lee, H.-J. Ahn, *J. Alloys Compd.* 682 (2016) 177–184.
- [11] S. Lee, Y.-W. Lee, D.-H. Kwak, J.-Y. Lee, S.-B. Han, J.I. Sohn, K.-W. Park, *J. Ind. Eng. Chem.* 43 (2016) 170–176.
- [12] L. Shang, H. Yu, X. Huang, T. Bian, R. Shi, Y. Zhao, G.I.N. Waterhouse, L.-Z. Wu, C.-H. Tung, T. Zhang, *Adv. Mater.* 28 (2016) 1668–1674.
- [13] L. Zhao, X.-L. Sui, J.-Z. Li, J.-J. Zhang, L.-M. Zhang, G.-S. Huang, Z.-B. Wang, *Appl. Catal. B Environ.* 231 (2018) 224–233.
- [14] Z. Hunag, H. Pan, W. Yang, H. Zhou, N. Gao, C. Fu, S. Li, H. Li, Y. Kuang, *ACS Nano* 12 (2018) 208–216.
- [15] Y. Zhang, W.-J. Jiang, L. Guo, X. Zhang, J.-S. Hu, Z. Wei, L.-J. Wan, *ACS Appl. Mater. Interfaces* 7 (2015) 11508–11515.
- [16] H. Zhong, Y. Luo, S. He, P. Tang, D. Li, N. Alonso-Vante, Y. Feng, *ACS Appl. Mater. Interfaces* 9 (2017) 2541–2549.
- [17] S. Ratto, I. Krusenbergh, M. Kaarik, M. Kook, R. Saar, P. Kanninen, T. Kallio, J. Leis,

- K. Tammeveski, Appl. Catal. B Environ. 219 (2017) 276–286.
- [18] Q. Wang, Z. Chen, N. Wu, B. Wang, W. He, Y. Lei, Y. Wang, Chemelectrochem 4 (2017) 514–520.
- [19] D.-H. Kwak, S.-B. Han, Y.-W. Lee, H.-S. Park, I.-A. Choi, M.-C. Kim, S.-J. Kim, D.-H. Kim, J.-I. Son, K.-W. Park, Appl. Catal. B Environ. 203 (2017) 889–898.
- [20] D.-H. Kwak, S.-B. Han, D.-H. Kim, J.E. Won, K.-W. Park, Appl. Catal. B Environ. 238 (2018) 93–103.
- [21] S.h. Ahn, X. Yu, A. Manthiram, Adv. Mater. 29 (2017) 1606534.
- [22] C. Liu, J. Wang, J. Li, R. Luo, X. Sun, J. Shen, W. Han, L. Wang, Carbon 114 (2017) 706–716.
- [23] L. Osmieri, R. Escudero-Cid, A.H.A.M. Videla, P. Ocon, S. Specchia, Appl. Catal. B Environ. 201 (2017) 253–265.
- [24] Y. Li, C. Guo, J. Li, W. Liao, Z. Li, J. Zhang, C. Chen, Carbon 119 (2017) 201–210.
- [25] Y. Mun, M.J. Kim, S.-A. Park, E. Lee, Y. Ye, S. Lee, Y.-T. Kim, S. Kim, O.-H. Kim, Y.-H. Cho, Y.-E. Sung, J. Lee, Appl. Catal. B Environ. 222 (2018) 191–199.
- [26] H.B. Yang, J. Miao, S.-F. Hung, J. Chen, H.B. Tao, X. Wang, L. Zhang, R. Chen, J. Gao, H.M. Chen, L. Dai, B. Liu, Sci. Adv. 2 (2016) e1501122.
- [27] M. Sun, D. Davenport, H. Liu, J. Qu, M. Elimelech, J. Li, J. Mater. Chem. A 6 (2018) 2527–2539.
- [28] D. Shin, B. Jeong, B.S. Mun, H. Jeon, H.-J. Shin, J. Baik, J. Lee, J. Phys. Chem. C 117 (2013) 11619–11624.
- [29] C. Li, F. Sun, Y. Lin, J. Power Sources 384 (2018) 48–57.
- [30] G.-H. An, D.-Y. Lee, H.-J. Ahn, ACS Appl. Mater. Interfaces 9 (2017) 12478–12485.
- [31] G.-H. An, D.-Y. Lee, Y.-J. Lee, H.-J. Ahn, ACS Appl. Mater. Interfaces 8 (2016) 30264–30270.
- [32] G.-H. An, D.-Y. Lee, H.-J. Ahn, ACS Appl. Mater. Interfaces 8 (2016) 19466–19474.
- [33] L. Lin, Q. Zhu, A.-W. Xu, J. Am. Chem. Soc. 136 (2014) 11027–11033.
- [34] X. Yuan, H. Ge, X. Liu, X. Wang, W. Chen, W. Dong, F. Huang, J. Alloys Compd. 688 (2016) 613–618.
- [35] H. Tan, J. Tang, J. Henzie, Y. Li, X. Xu, T. Chen, Z. Wang, J. Wang, Y. Ide, Y. Bando, Y. Yamauchi, ACS Nano 12 (2018) 5674–5683.
- [36] G.M.K. Abotsi, A.W. Scaroni, Carbon 28 (1990) 79–84.
- [37] Y. Yamazaki, T. Gettongsong, M. Mikawa, Y. Amano, M. Machida, J. Fiber Sci. Technol. 72 (2016) 237–243.
- [38] I. Kone, A. Xie, Y. Yang, Y. Chen, J. Liu, Y. Chen, Y. Sun, X. Yang, P. Wan, ACS Appl. Mater. Interfaces 9 (2017) 20963–20973.
- [39] G. Ren, X. Lu, Y. Li, Y. Zhu, L. Dai, L. Jiang, ACS Appl. Mater. Interfaces 8 (2016) 4118–4125.
- [40] S. Lee, D.-H. Kwak, S.-B. Han, Y.-W. Lee, J.-Y. Lee, I.-A. Choi, H.-S. Park, J.-Y. Park, K.-W. Park, ACS Catal. 6 (2016) 5095–5102.
- [41] G.-H. An, Y.-G. Lee, H.-J. Ahn, J. Alloys Compd. 764 (2018) 416–423.
- [42] Y.-G. Lee, G.-H. An, H.-J. Ahn, J. Alloys Compd. 751 (2018) 62–68.
- [43] K. Yuan, S. Sfaelou, M. Qiu, D. Lutzenkirchen-Hecht, X. Zhuang, Y. Chen, C. Yuan, X. Feng, U. Scherf, ACS Energy Lett. 3 (2018) 252–260.
- [44] G. Panomsuwan, N. Saito, T. Ishizaki, J. Mater. Chem. A 3 (2015) 9972–9981.
- [45] S. Chen, J. Bi, Y. Zhao, L. Yang, C. Zhang, Y. Ma, Q. Wu, X. Wang, Z. Hu, Adv. Mater. 24 (2012) 5593–5597.
- [46] Y. Wang, H. Liu, K. Wang, S. Song, P. Tsiakaras, Appl. Catal. B Environ. 210 (2017) 57–66.
- [47] L. Zhang, Z. Xia, J. Phys. Chem. C 115 (2011) 11170–11176.
- [48] S. Lee, D.-H. Kwak, S.-B. Han, E.-T. Hwang, M.-C. Kim, J.-Y. Lee, Y.-W. Lee, K.-W. Park, Electrochim. Acta 191 (2016) 805–812.
- [49] W. Wei, X. Shi, P. Gao, S. Wang, W. Hu, X. Zhao, Y. Ni, X. Xu, Y. Xu, W. Yan, H. Ji, M. Cao, Nano Energy 52 (2018) 29–37.
- [50] S. Jiang, Y. Sun, H. Dai, J. Hu, P. Ni, Y. Wang, Z. Li, Z. Li, Nanoscale 7 (2015) 10584–10589.
- [51] X. Sun, P. Song, T. Chen, J. Liu, W. Xu, Chem. Commun. 49 (2013) 10296–10298.
- [52] G. Liu, X. Li, J.-W. Lee, B.N. Popov, Catal. Sci. Technol. 1 (2011) 207–217.